Nanoscale Advances

ROYAL SOCIETY OF CHEMISTRY

PAPER

View Article Online
View Journal | View Issue

Cite this: *Nanoscale Adv.*, 2020, **2**, 2808

Ultrafast lattice and electronic dynamics in single-walled carbon nanotubes†

Dingguo Zheng, ‡[ab] Chunhui Zhu,‡[a] Zian Li,[a] Zhongwen Li, [a] Jun Li,[a] Shuaishuai Sun, [a] Yongzhao Zhang,[ab] Fengqiu Wang, [e] Huanfang Tian,[a] Huaixin Yang [abcd] and Jianqi Li*[abc]

Received 5th April 2020
Accepted 21st May 2020

DOI: 10.1039/d0na00269k

rsc.li/nanoscale-advances

Understanding the photoinduced ultrafast structural transitions and electronic dynamics in single-walled carbon nanotubes (SWCNTs) is important for the development of SWCNT-based optoelectronic devices. In this study, we conducted femtosecond-resolved electron diffraction and electron energy-loss spectroscopy (EELS) measurements on SWCNTs using ultrafast transmission electron microscopy. The experimental results demonstrated that dominant time constants of the dynamic processes were ~1.4 ps for electron-driven lattice expansion, ~17.4 ps for thermal phonon-driven lattice expansion associated with electron–phonon coupling. The time-resolved EELS measurements clearly revealed a notable red shift of plasmon peaks by ~100 meV upon femtosecond laser excitation. Different features of charge carrier excitation and relaxation were carefully discussed in correlation with the lattice dynamics and photoinduced absorption signals of SWCNTs. Our results provide a comprehensive understanding of the ultrafast dynamics in SWCNTs and powerful techniques to characterize the dynamics of low-dimensional structures.

Introduction

Single-walled carbon nanotubes (SWCNTs) have been studied extensively as important low-dimensional materials. SWCNTs exhibit a rich variety of physical properties that are attractive for many optoelectronic and photonics applications, such as light harvesting, high-speed photodetection, and ultrafast all-optical modulation.[1–5] Certain optical properties of SWCNTs have been explained by a combination of exciton effects and the red tail of π-plasmon resonance.[6–9] However, the physical mechanisms behind the ultrafast optical responses of SWCNTs are still not fully understood.

Transient absorption (TA) spectroscopy is a useful tool for studying ultrafast optical processes.[10] Numerous TA spectroscopy experiments on SWCNTs have provided information about their electronic dynamic features; *e.g.*, biexciton and exciton annihilation.[11–16] However, the plasmonic and lattice dynamics of SWCNTs cannot be directly revealed by TA spectroscopy with probe wavelengths in the visible to infrared range. Several independent investigations have demonstrated that ultrafast behaviors of plasmons and the lattice may strongly affect the ultrafast features of SWCNTs.[11,13,17] Electron energy-loss spectroscopy (EELS) has been used to study the plasmonic properties of SWCNTs and revealed certain prominent features of tubular structures.[8,9] Unfortunately, few time-resolved EELS experiments on photoinduced plasmonic dynamics in SWCNTs and dynamic changes of lattice structures have been performed to date. The structural dynamics of nanotubes is still an important issue that is under investigation.[18,19] For example, time-resolved Raman spectroscopy of SWCNTs showed the notable evolution of phonon population and the lattice dynamics of multi-walled carbon nanotubes (MWCNTs) have been extensively investigated using ultrafast X-ray diffraction and ultrafast electron diffraction (UED).[18,20–22] In particularly, the correlation between the structure dynamics and electronic dynamics has been never directly revealed.

Herein, we using ultrafast transmission electron microscope (UTEM) perform time-resolved EELS and UED measurements on SWCNTs. Both electronic and lattice structures of the SWCNTs show notable dynamic changes after femtosecond laser excitation. The general signatures in TA spectra of SWCNTs are also investigated. It is demonstrated that the photoinduced absorption (PA) signals could be correlated with the red shift of π plasmons and other contributions.

[a]Beijing National Laboratory for Condensed Matter Physics, Institute of Physics, Chinese Academy of Sciences, Beijing, 100190, China. E-mail: ljq@aphy.iphy.ac.cn
[b]School of Physical Sciences, University of Chinese Academy of Science, Beijing, 100190, China
[c]Yangtze River Delta Physics Research Center Co., Ltd., Liyang, Jiangsu, 213300, China
[d]Songshan Lake Materials Laboratory, Dongguan, Guangdong, 523808, China
[e]School of Electronic Science and Engineering, Collaborative Innovation Center of Advanced Microstructures, Nanjing University, Nanjing 210093, China

† Electronic supplementary information (ESI) available. See DOI: 10.1039/d0na00269k

‡ These authors contributed equally to this work.

Results and discussion

Lattice dynamics

Sample preparation and experimental measurement details are presented in the Experimental section (ESI†). The SWCNT samples were a mixture of metallic and semiconducting types with diameters of 1.2–1.7 nm. For UTEM observation, the SWCNTs were dispersed on 2000-mesh copper (Cu) grids by solution processing. As shown in Fig. S1,† the SWCNTs existed as bunched structures with random tube orientation. A typical EELS profile of a SWCNT sample is shown in Fig. S2,† illustrating the characteristic peaks of the SWCNTs. The UED measurements were performed using our custom-built UTEM developed based on a JEOL-2000EX microscope. The dynamic processes were initiated by a 520 nm pump laser with a fluence of ~47 mJ cm^{-2}, repetition rate of ~100 kHz, and duration of ~300 fs.

As shown in Fig. 1, the microstructure of the SWCNT sample was characterized. Fig. 1a shows a typical 2D diffraction pattern of SWCNTs. The two Debye–Scherrer rings were attributed to the (100) and (110) lattice planes. For comparison, we also show an electron diffraction pattern of MWCNTs in Fig. 1b, which contains a strong (002) reflection ring. To facilitate data analysis, the SWCNT diffraction pattern was transformed into a 1D profile by azimuthal integration and subsequent background subtraction (Fig. 1c). An atomic model of an armchair tube is shown in Fig. 1d, in which the (100) and (110) crystal planes are indicated.

A series of UED patterns at different time delays were obtained to reveal the lattice dynamics of SWCNTs. In Fig. 2a, we show two typical diffraction profiles obtained before (−10 ps) and after time zero (200 ps). After femtosecond-laser excitation, the lattice spacings of the (100) and (110) planes increase, whereas diffraction intensity shows a visible decrease. The peak position of the (100) plane as functions of short and long-time delays is shown in Fig. 2b and c, respectively. The (100) lattice spacing reaches a maximum value at a time delay of ~5 ps. In

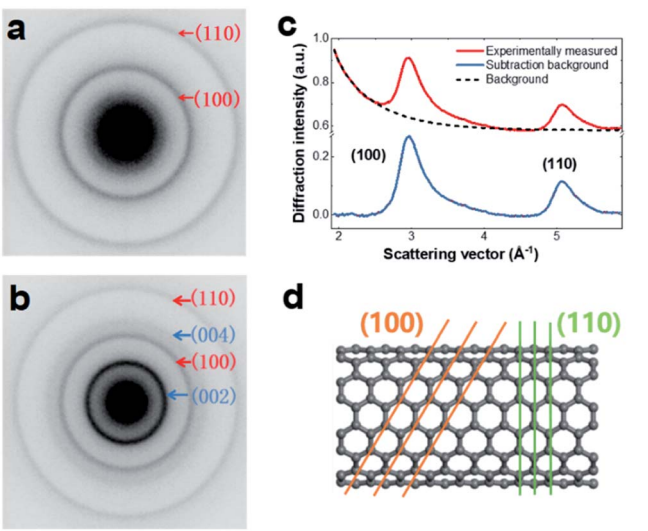

Fig. 1 Electron diffraction patterns and structural model of SWCNTs. (a) Typical pulsed electron diffraction pattern of SWCNTs investigated by a 4D electron microscope. (b) Electron diffraction pattern of MWCNTs for comparison; the strong [002] diffraction ring is indicated. (c) 1D electron diffraction profiles obtained by azimuthally averaging the 2D SWCNT diffraction pattern. The red curve is the original data and the background (dashed line) has been subtracted in the blue curve. (d) Atomic model of an armchair-type SWCNT with (100) and (110) lattice plane indexes.

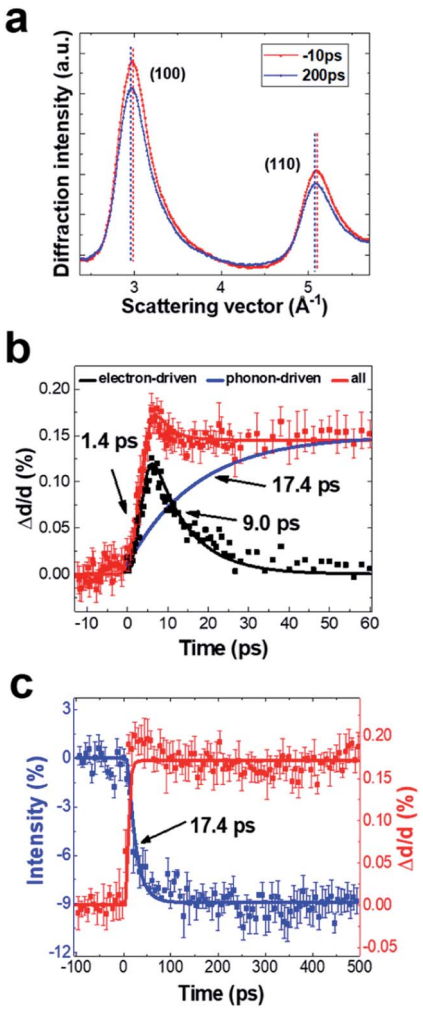

Fig. 2 Structural changes of SWCNTs exposed to a pump fluence of 47 mJ cm^{-2}. (a) 1D profiles of ultrafast diffraction patterns taken before and after femtosecond laser excitation. Dashed lines indicate a shift of peak position. (b) Evolution of the (100) planar distance in the time span from −10 to 60 ps. The red squares are experimental data, the red solid curve shows the theoretical data with a biexponential function. $\Delta d/d$ is defined as $\Delta d/d = [s(0) - s(t)]/s(0)$, where $s(t)$ is the peak position (scattering vector) and d is lattice spacing. The blue solid curve represents the phonon contribution to the lattice expansion. Black squares represent non-thermal electron-driven expansion, which is extracted from the red squares by subtracting a fitted data with the time constant 17.4 ps that obtained from diffraction intensity curve in (c). The black solid curve is the theoretical fitting data with a biexponential function. (c) Diffraction intensity and peak shift as functions of time delay at a long-time scale. The blue squares represent intensity evolution and the red squares represent the peak position shift. Solid curves (blue and red) show the theoretical data with a single exponential function.

addition, we also observed a fast decay signal (<30 ps) and long-lived signal (>500 ps) accompanied with clear lattice expansion. The long-lived signal shows similar features to the thermal phonon-driven process in MWCNTs,[18,20–22] which can be well described by a single exponential process, as demonstrated by the two-temperature mode.[23] During this process, energy transforms from the hot electrons to the lattice by strongly coupled optical phonons,[24,25] resulting in a quick increase of lattice temperature and a decrease of the diffraction intensity according to the Debye–Waller factor. Fig. 2c shows the diffraction intensity as a function of time delay, illustrating the intensity decrease with a time constant of ~17.4 ps after laser excitation. We consider that the lattice plane expands by about 0.15%, so C–C bond length is estimated to increase by 0.21 pm (C–C bond length is ~1.421 Å). The lattice temperature rise was estimated to be ~800 K using an axial thermal expansion coefficient of 2×10^{-6} K^{-1}.[26]

The fast components on the picosecond time scale are electron-driven lattice expansion processes, which are caused by the depopulation of electrons in the π- and σ-bonds upon femtosecond laser excitation.[18–22] To isolate these non-thermal components, we subtracted the phonon-driven process (Fig. 2c), as shown in Fig. 2b. Careful analysis on the electron-driven transient state revealed that this fast process can be well characterized by an exponential increase with a time constant of ~1.4 ps and then the relaxation time was about ~9.0 ps. We also extracted information about the (110) plane dynamics from the time-resolved electron diffraction data, as displayed in Fig. S3.† The fundamental changes of the (110) plane showed similar features to those obtained for the (100) plane, although the lattice expansion along the [110] direction was slightly slower than that along the [100] direction. In addition, the intensity of the (100) diffraction peak decreased more than that of the (110) diffraction peak. This phenomenon can be well explained by the Debye–Waller factor ($W(t)$):[27]

$$\ln\left[\frac{I(t)}{I(0)}\right] = -2W(t) = -\frac{\boldsymbol{s}^2\delta\boldsymbol{u}^2(t)}{3},$$

where $I(t)$ is the diffraction peak intensity at a given time t, $\boldsymbol{s}$ is the scattering vector, and $\delta\boldsymbol{u}^2(t)$ is the mean square of atomic displacement. The (110) plane has a bigger $\boldsymbol{s}$, which can yield a greater intensity decrease associated with a temperature rise after femtosecond laser excitation, than that of the (100) plane. It is worth pointing out that the major time constants observed for the SWCNTs were different from those observed for MWCNTs.[18,21] For example, the thermal phonon-driven lattice expansion took a much longer time for the SWCNTs than for the MWCNTs, which suggests that alteration of the dimensionality and interlayer coupling of nanosystems can have an evident effect on their dynamic nature. In addition, no signature about the radial breathing mode and G-mode of SWCNTs are found in our UED measurements.[28,29]

Electronic dynamics

Fig. 3 presents the time-resolved EELS results obtained under similar experimental conditions to those used for the UED measurements. The low-loss EELS profile of the SWCNTs is shown in Fig. 3a. The plasmonic peaks observed at ~5.0 and 22.4 eV can be attributed to the π and π + σ plasmons of SWCNTs, respectively.[8,30,31] Fig. 3b and c show shifts of the π and π + σ plasmonic peaks as functions of time delay. The maximum peak shifts were observed at a time delay of about 1 ps. Careful measurements showed that these electronic dynamic transitions firstly recovered by a fast process with a time constant of ~2.0 ps, and then followed by a long-lived red-shifted signal. It is also known that photon-induced near-field electron microscopy (PINEM) signals of SWCNTs appear in the femtosecond time domain after femtosecond laser pumping. Therefore, the rising time of the curves in Fig. 3 could contain certain error. However, the PINEM signals disappeared after ~0.6 ps, so they had no visible influence on the main process of the plasmon peaks.

According to a theoretical study of 1D systems, the plasmon resonance energy E_p in SWCNTs is correlated with the resonance frequency ω_p and density of valence electrons N as follows,[32]

$$E_p = \hbar\omega_p = \hbar\sqrt{\frac{Ne^2}{m\varepsilon_0}} \quad (1)$$

$$N = \frac{64\pi r}{3a^2(2r + d_D)^2} \quad (2)$$

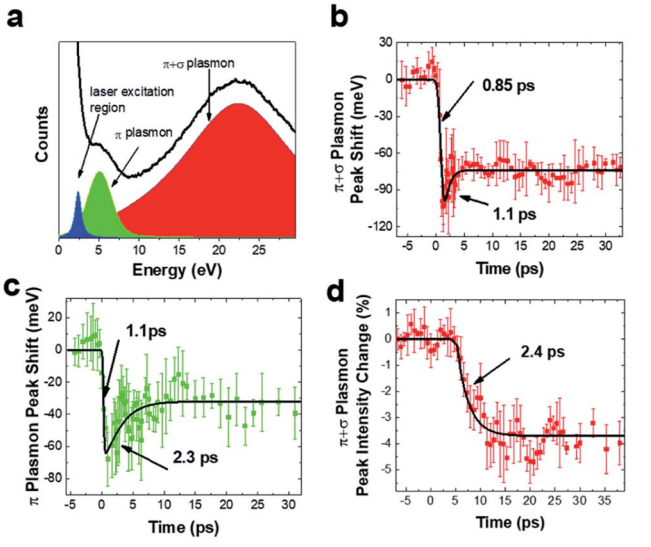

Fig. 3 Time-resolved EELS of SWCNT that exposed to a pump fluence of 44 mJ cm^{-2}. (a) Static EELS profile of SWCNTs (black line). The red region (band located at ~22.4 eV) represents π + σ plasmons. The green region (band located at ~5 eV) represents π plasmons. (b) Time dependence of the π + σ plasmon peak energy shift after laser excitation. The π + σ plasmon peak shows a rapid fall process (~100 meV), then a small rise process, and finally reaches a quasi-steady state with a red shift of about 75 meV. (c) Time dependence of the π plasmon peak energy shift. The rapid fall process (~65 meV) and finally reaches a quasi-steady state process (~35 meV) similar to the π + σ plasmon peak energy shift. (d) π + σ plasmon peak intensity change, which shows a 3.5% decrease in amplitude and a time constant of 2.4 ps.

where $\hbar$ is the Planck constant, e is the charge of an electron, m is the effective mass of an electron, ε_0 is the dielectric permittivity of vacuum, r is the radius of SWCNTs, a is the lattice constant in the graphitic sheet, and d_D is the distance between two neighboring SWCNTs. It is intuitive to attribute the red shift of plasmonic peaks to the decrease of N. The green pump laser promoted electron transfer from the valence (π) band to the conduction (π^*) band and these photocarriers reduce electrons participate in the formation of π and $\pi + \sigma$ plasmons, reflecting the fast red shift of the plasmons. Depopulation of the π and $\pi + \sigma$ plasmons also weakened the chemical bonding of carbons, as demonstrated by the electron-driven lattice expansion. Such photocarriers relaxed from the π^* to π bands with a typical time constant of ~1–2 ps after femtosecond laser excitation.[17] π and $\pi + \sigma$ plasmons partially recovered from the exited states, as clearly shown in Fig. 3b and c. Moreover, the reconfiguration of hot electron carriers resulted in further alteration of chemical bonds and lattice expansion.

The lattice expansion may bring in another factor that affects the plasmon resonance. The maximum lattice expansion, as shown in Fig. 2b, was only ~1.5‰ and a plasmon red shift of ~37 meV was calculated from eqn (1) and (2) using the parameters of $r = 0.7$ nm, $a = 0.246$ nm, and $d_D = 0.34$ nm (both r and a increase 1.5‰). This suggests that lattice expansion partially responsible for the long-lived red shift of plasmons with a typical value of several tens of millielectronvolts. Our UTEM sample contained bundles of nanotubes, so d_D may also play the other role in the plasmonic dynamics after femtosecond laser excitation, as reported in studies of MWCNTs, in which the interlayer space of carbon sheets is noticeably enlarged following laser excitation because of the weak van der Waals bonding.[18,20–22] We estimated the red shift of the plasmon peak using eqn (1) and (2) and obtained a change of the resonance frequency of ~73 meV upon increasing d_D by 1%, r and a by 1.5‰ (the radial expansion observed in MWCNTs is ~2.5% at fluence of 44 mJ cm^{-2}).[18,21,22] This result is in agreement with the experimental data discussed above. It should be pointed out that the long-lived trapped photocarriers, which are often located at defect sites and interfaces, could also contribute to the electronic process in the present system, as discussed elsewhere.[10] Moreover, our careful analysis also revealed that the intensity of $\pi + \sigma$ plasmons decreased (~3.5%) with a time constant of ~2.4 ps, as illustrated in Fig. 3d. This alteration is likely correlated with the increase of lattice temperature induced *via* electron–phonon coupling, which occurs on the time scale of a few picoseconds.

The red shift of π plasmons can impact the ultrafast photoresponse of SWCNTs.[33,34] To illustrate this point, we reproduced the absorbance of SWCNTs by four Gaussian using the data in literature.[35] As shown in Fig. S4,† a 10 meV shift of π-plasmon resonance can already rise a few percent absorbance change for SWCNTs in visible to IR wavelength. In particularly, it is found that the enhance of absorbance in nonresonant range is much larger than that in resonant range. We performed broadband TA spectroscopy measurements on SWCNT samples with 1.55 eV pumping and 0.5–1.3 eV probing. The sample was dispersed on a quartz substrate and the pump fluence was fixed

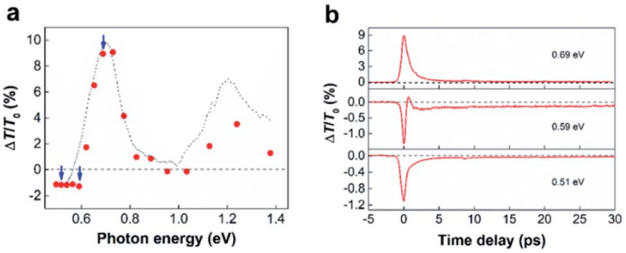

Fig. 4 Optical experimental results showing the general signatures of TA spectra of SWCNTs. (a) Broadband signals at time zero and (b) time-resolved traces at three selected probe energies. The dotted line in (a) exhibits a profile of linear absorbance of SWCNTs and the dashed horizontal line is a visual guide.

at ~3 mJ cm^{-2} (Fig. 4) and 0.1 mJ cm^{-2} (Fig. S5†). Similar to previous reported results,[12,13,33,36,37] two PA bands in the nonresonant range and two PB (photon bleaching) in the resonant range are observed in the TA spectroscopy (Fig. 4a). As demonstrated in the previous works, we attribute the PB signal to the state filling effects.[10–13] The optical transition with ~1.6 eV excitation occurs at energy level higher than the second excitonic transitions (S_{22}). In this case, photocarrier would transfer to the S_{22} and first excitonic transition (S_{11}) very fast by intratube relaxation, which fill the states of S_{11} and S_{22}, thus leading to two PB bands. In addition, intertube energy transfer usually occurs in SWCNT bundles,[38] and this process also contributes to the exciton population redistribution. Although the redshift of the π-plasmon resonance can be attribute to the PA signals, we believe that there are multiple physical mechanisms behind these PA signals. This can be confirmed by a clear delay time-dependent PA–PB–PA transition observed at a probing energy of ~0.59 eV in Fig. 4b. Besides the redshift of the π-plasmon resonance, PA signals have been described by different mechanisms including, intersubband transitions,[39] multiple-exciton formation,[13,37,40,41] dark-bright exciton transitions,[42] charge induced Stark effect[43] and carrier-hot phonon coupling[17] *etc.* Based on the results in Fig. 4, it hard to completely certain which one is responsible to the two PA bands. However, considering the pump fluence is very high, multiple-exciton coupling (biexciton, triexciton, and exciton annihilation) may be occurred.[13,37,40,41] No blue-shifted PA signal may exclude the dark-bright exciton transitions,[42] but we cannot rule out any charge induced Stark effect and carrier-hot phonon coupling effects.[17,43] Furthermore, the intertube energy relaxation can result a large exciton population in the SWCNTs with low energy exciton resonant states, thus leading to a more significant PA signal at red side of S_{11}. Notably, the ultrafast dynamics in SWCNTs is strong pump fluence dependent,[44,45] resulting in that TR-EELS results and TA spectroscopy cannot directly compare. Nonetheless, a solid experimental evidence for the redshift of π plasmons still helpful to understand the ultrafast optical response in SWCNTs.

Finally, we briefly discuss the dynamic processes and transient states in photoexcited SWCNTs based on the measured lattice structural evolution and photophysical properties. For ultrafast investigations, the nonequilibrium states are

initialized with an ultrashort laser pulse typically in the visible to infrared region. Considering the large bandgap of the σ band in SWCNTs, the laser pulse will promote electrons from the π band to the π* band. In other words, optical excitation leads to electron depopulation of the valence band and an increase of the electron population in the conduction band. Such an electron population change can directly result in Pauli blocking effects, which account for PB signals in TA spectroscopy. Other electronic effects, *e.g.*, the red shift of plasmons and photoinduced multiple-exciton formation, also occur during or immediately after laser excitation. Then, the photocarriers will relax to the ground state with a lifetime of about 1–2 ps, which contributes to the fast decay at short time delay in both ultrafast optical spectroscopy and time-resolved EELS. It should be noted that during these electronic processes, electron-driven lattice expansion is also activated by electron depopulation of the π band. Electron-driven expansion exhibits a build-up time of ∼1–2 ps and a decay time of several picoseconds (∼9.0 ps in this paper). Thermal phonon-driven lattice expansion is established with a characteristic time ∼17 ps, then leave a quasi-equilibrium state lasts more than 500 ps.

Experiment

Sample preparation

High-purity SWCNTs (>99%) dissolved in aqueous surfactant solution were purchased from Nanjing XFNANO Materials Technology Corporation Limited, Nanjing, China. The SWCNTs were a mixture of metallic and semiconducting types with diameters of 1.2–1.7 nm and lengths of 300 nm to 4 μm. To prepare UTEM samples, SWCNTs were diluted in distilled water and then sonicated for 10 min. The solution was added dropwise onto a 2000-mesh Cu grid and then dried by annealing at 90 °C for 30 min. A 400-mesh Cu grid was placed on top of the 2000-mesh Cu grid to form a sandwich structure to enhance mechanical stability and heat conduction for UTEM experiments.

UED experiment

The UED experiments were performed in the UTEM developed based on a JEOL-2000EX (JEOL Inc.) microscope.[21,22,46] The original laser beam (λ = 1040 nm, full width at half-maximum = 300 fs) was split into two paths; one was frequency-quadrupled and focused to the LaB_6 cathode to obtained pulsed electrons and the other was frequency-doubled and focused on the sample with a beam diameter ∼50 μm to excite dynamic processes. The pulsed electrons were accelerated to 160 keV and then focused to a beam diameter of ∼20 μm on the sample. Considering the heat dispersion of the UTEM sample and the signal-to-noise ratio, a laser repetition frequency of 100 kHz was used in our measurements. The diffraction patterns were recorded by a charge coupled device with an exposure time of ∼5 s. The temporal resolution of the ultrafast UED experiments is ∼800 fs. No distinct optical damage and heat accumulation effects were observed in these experimental conditions.

Time-resolved EELS experiment

The time-resolved EELS measurement was performed using another UTEM that was developed based on a JEOL-2100F (JEOL Inc.) microscope with a field-emission gun.[47] In this setup, the original laser beam had a pulse width of ∼190 fs and a central wavelength of ∼1030 nm. The diameter of the laser beam on the sample was ∼38 μm with a fluence of ∼44 mJ cm^{-2}. A laser repetition frequency of 200 kHz was used in the time-resolved EELS measurement. No object aperture was inserted into the electron optical system; the collection angle was estimated to be more than 100 mrad. A Gatan spectrometer (GIF 965) was used to record the EELS and an exposure time of 50 s was used in the time-resolved measurement. The zero-loss peak center and plasmon peak center were determined by gravity arithmetic. The temporal resolution of the ultrafast TR-EELS experiments is ∼500 fs.

TA spectroscopy

An 800 nm (∼1.55 eV) 1 kHz Ti:sapphire amplifier (Libra, Coherent Inc.) was used as a laser source. Infrared (0.5–1.3 eV) pulses were generated by a feeding 800 nm pulses into an optical parametric amplifier system (OPA-SOLO, Coherent Inc.). The pump-induced differential transmission changes were recorded by a photodetector and lock-in amplifier referenced to a 334 Hz chopped pump.

Conclusions

Ultrafast dynamics in SWCNTs were investigated by combining measurements of time-resolved EELS, UED, and TA spectroscopy. Importantly, a red shift of plasmons approaching 100 meV and clear lattice expansion of the SWCNTs were observed upon femtosecond laser excitation. The non-thermal transient and thermal-phonon driving changes in the SWCNTs were addressed based on measurements of electronic and lattice temporal changes. Considering general signatures in TA spectroscopy, we carefully discussed the relevant transient states on time scales of femtoseconds to hundreds of picoseconds. Our study firstly discusses the correlation between the structural transients and electronic dynamics. Emerging UTEM techniques have the potential to markedly improve our understanding of the dynamics of low-dimensional materials.

Conflicts of interest

There are no conflicts to declare.

Acknowledgements

This work was supported by the National Key Research and Development Program of China (Grant No. 2016YFA0300303, 2017YFA0504703, 2017YFA0302904, and 2017YFA0303000), the National Basic Research Program of China (Grant No. 2015CB921304), the National Natural Science Foundation of China (Grant No. 11774391, 11774403, and 11804381), the Strategic Priority Research Program (B) of the Chinese Academy

of Sciences (Grant No. XDB25000000 and XDB33000000), the Scientific Instrument Developing Project of the Chinese Academy of Sciences (Grant No. ZDKYYQ20170002), and the China Postdoctoral Science Foundation funded project (Grant No. BX20180351). We thank Natasha Lundin, PhD, from Liwen Bianji, Edanz Editing China (http://www.liwenbianji.cn/ac), for editing the English text of a draft of this manuscript.

References

1 P. Avouris, M. Freitag and V. Perebeinos, *Nat. Photonics*, 2008, **2**, 341–350.
2 M. F. L. De Volder, S. H. Tawfick, R. H. Baughman and A. J. Hart, *Science*, 2013, **339**, 535–539.
3 T. Hasan, Z. Sun, F. Wang, F. Bonaccorso, P. H. Tan, A. G. Rozhin and A. C. Ferrari, *Adv. Mater.*, 2009, **21**, 3874–3899.
4 A. Martinez and Z. Sun, *Nat. Photonics*, 2013, **7**, 842–845.
5 L.-M. Peng, Z. Zhang and C. Qiu, *Nat. Electron.*, 2019, **2**, 499–505.
6 M. J. O'Connell, S. M. Bachilo, C. B. Huffman, V. C. Moore, M. S. Strano, E. H. Haroz, K. L. Rialon, P. J. Boul, W. H. Noon, C. Kittrell, J. Ma, R. H. Hauge, R. B. Weisman and R. E. Smalley, *Science*, 2002, **297**, 593–596.
7 F. Wang, G. Dukovic, L. E. Brus and T. F. Heinz, *Science*, 2005, **308**, 838–841.
8 R. Kuzuo, M. Terauchi and M. Tanaka, *Jpn. J. Appl. Phys.*, 1992, **31**, L1484–L1487.
9 M. F. Lin and K. W. Shung, *Phys. Rev. B: Condens. Matter Mater. Phys.*, 1994, **50**, 17744–17747.
10 G. Soavi, F. Scotognella, G. Lanzani and G. Cerullo, *Adv. Opt. Mater.*, 2016, **4**, 1670–1688.
11 Y.-Z. Ma, J. Stenger, J. Zimmermann, S. M. Bachilo, R. E. Smalley, R. B. Weisman and G. R. Fleming, *J. Chem. Phys.*, 2004, **120**, 3368–3373.
12 O. J. Korovyanko, C.-X. Sheng, Z. V. Vardeny, A. B. Dalton and R. H. Baughman, *Phys. Rev. Lett.*, 2004, **92**, 017403.
13 G. N. Ostojic, S. Zaric, J. Kono, V. C. Moore, R. H. Hauge and R. E. Smalley, *Phys. Rev. Lett.*, 2005, **94**, 097401.
14 L. Lüer, S. Hoseinkhani, D. Polli, J. Crochet, T. Hertel and G. Lanzani, *Nat. Phys.*, 2008, **5**, 54–58.
15 D. Stich, F. Späth, H. Kraus, A. Sperlich, V. Dyakonov and T. Hertel, *Nat. Photonics*, 2013, **8**, 139–144.
16 S. Xu, F. Wang, C. Zhu, Y. Meng, Y. Liu, W. Liu, J. Tang, K. Liu, G. Hu, R. C. Howe, T. Hasan, R. Zhang, Y. Shi and Y. Xu, *Nanoscale*, 2016, **8**, 9304–9309.
17 C. Zhu, Y. Liu, J. Xu, Z. Nie, Y. Li, Y. Xu, R. Zhang and F. Wang, *Sci. Rep.*, 2017, **7**, 11221.
18 G. M. Vanacore, R. M. van der Veen and A. H. Zewail, *ACS Nano*, 2015, **9**, 1721–1729.
19 T. Jiang, H. Hong, C. Liu, W. T. Liu, K. Liu and S. Wu, *Nano Lett.*, 2018, **18**, 2590–2594.
20 S. T. Park, D. J. Flannigan and A. H. Zewail, *J. Am. Chem. Soc.*, 2012, **134**, 9146–9149.
21 G. Cao, S. Sun, Z. Li, H. Tian, H. Yang and J. Li, *Sci. Rep.*, 2015, **5**, 8404.
22 S. Sun, Z. Li, Z. A. Li, R. Xiao, M. Zhang, H. Tian, H. Yang and J. Li, *Nanoscale*, 2018, **10**, 7465–7471.
23 J. Hohlfeld, S.-S. Wellershoff, J. Güdde, U. Conrad, V. Jähnke and E. Matthias, *Chem. Phys.*, 2000, **251**, 237–258.
24 T. Kampfrath, L. Perfetti, F. Schapper, C. Frischkorn and M. Wolf, *Phys. Rev. Lett.*, 2005, **95**, 187403.
25 O. A. Dyatlova, C. Köhler, E. Malic, J. Gomis-Bresco, J. Maultzsch, A. Tsagan-Mandzhiev, T. Watermann, A. Knorr and U. Woggon, *Nano Lett.*, 2012, **12**, 2249–2253.
26 H. Jiang, B. Liu, Y. Huang and K. C. Hwang, *J. Eng. Mater. Technol.*, 2004, **126**, 265–270.
27 F. Carbone, D. S. Yang, E. Giannini and A. H. Zewail, *Proc. Natl. Acad. Sci. U. S. A.*, 2008, **105**, 20161–20166.
28 A. Gambetta, C. Manzoni, E. Menna, M. Meneghtti, G. Cerullo, G. Lanzani, S. Tretiak, A. Piryatinski, A. Saxena, R. L. Martin and A. R. Bishop, *Nat. Phys.*, 2006, **21**, 515–520.
29 L. Lüer, C. Gadermaier, J. Crochet, T. Hertel, D. Brida and G. Lanzani, *Phys. Rev. Lett.*, 2009, **102**, 127401.
30 F. S. Hage, T. P. Hardcastle, A. J. Scott, R. Brydson and Q. M. Ramasse, *Phys. Rev. B*, 2017, **95**, 195411.
31 M. Knupfer, T. Pichler, M. S. Golden, J. Fink, A. Rinzler and R. E. Smalley, *Carbon*, 1999, **37**, 733–738.
32 R. Kuzuo, M. Terauchi, M. Tanaka and Y. Saito, *Jpn. J. Appl. Phys.*, 1994, **33**, L1316–L1319.
33 J. S. Lauret, C. Voisin, G. Cassabois, C. Delalande, P. Roussignol, O. Jost and L. Capes, *Phys. Rev. Lett.*, 2003, **90**, 057404.
34 Y. Long, L. Song, C. Li, C. Zhang, G. P. Wang, S. Xie, L. Wang, P. Fu and Z. Zhang, *Chem. Phys. Lett.*, 2005, **405**, 300–303.
35 M. E. Itkis, D. E. Perea, R. Jung, S. Niyogi and R. C. Haddon, *J. Am. Chem. Soc.*, 2005, **127**, 3439–3448.
36 L. Lüer, G. Lanzani, J. Crochet, T. Hertel, J. Holt and Z. V. Vardeny, *Phys. Rev. B: Condens. Matter Mater. Phys.*, 2009, **80**, 205411.
37 D. J. Styers-Barnett, S. P. Ellison, B. P. Mehl, B. C. Westlake, R. L. House, C. Park, K. E. Wise and J. M. Papanikolas, *J. Phys. Chem. C*, 2008, **112**, 4507–4516.
38 L. Lüer, J. Crochet, T. Hertel, G. Cerullo and G. Lanzani, *ACS Nano*, 2010, **4**, 4265–4273.
39 C. Manzoni, A. Gambetta, E. Menna, M. Meneghetti, G. Lanzani and G. Cerullo, *Phys. Rev. Lett.*, 2005, **94**, 207401.
40 Y. Ma, L. Valkunas, S. L. Dexheimer, S. M. Bachilo and R. Fleming, *Phys. Rev. Lett.*, 2005, **94**, 157402.
41 S. M. Santos, B. Yuma, S. Berciaud, J. Shaver, M. Gallart, P. Gilliot, L. Cognet and B. Lounis, *Phys. Rev. Lett.*, 2011, **107**, 187401.
42 Z. Zhu, J. Crochet, M. S. Arnold, M. C. Hersam, H. Ulbricht, D. Resasco and T. Hertel, *J. Phys. Chem. C*, 2007, **111**, 3831–3835.
43 G. Soavi, F. Scotognella, D. Brida, T. Hefner, F. Späth, M. R. Antognazza, T. Hertel, G. Lanzani and G. Cerullo, *J. Phys. Chem. C*, 2013, **117**, 10849–10855.
44 J. Park, P. Deria, J. Olivier and M. J. Therien, *Nano Lett.*, 2014, **14**, 504–511.
45 L. Huang and T. D. Krauss, *Phys. Rev. Lett.*, 2006, **96**, 057407.
46 Z. Li, R. J. Xiao, P. Xu, C. Zhu, S. Sun, D. Zheng, H. Wang, M. Zhang, H. Tian, H. X. Yang and J. Q. Li, *ACS Nano*, 2019, **13**, 11623–11631.
47 C. Zhu, D. Zheng, H. Wang, M. Zhang, Z. Li, S. Sun, P. Xu, H. Tian, Z. Li, H. Yang and J. Li, *Ultramicroscopy*, 2020, **209**, 112887.